

Effect of Sr-doping on sinterability, morphology, structure, photocatalytic activity and AC conductivity of ZnO ceramics

T. Das¹ · B. K. Das¹ · K. Parashar¹ · R. Kumar² · H. K. Choudhary² ·
A. V. Anupama² · B. Sahoo² · P. K. Sahoo³ · S. K. S. Parashar¹

Received: 2 April 2017 / Accepted: 22 May 2017 / Published online: 8 June 2017
© Springer Science+Business Media New York 2017

Abstract The change in morphology, structure, catalytic activity and ac electrical conductivity of the Sr-doped ZnO ($\text{Zn}_{1-x}\text{Sr}_x\text{O}$, $x=0, 0.01, 0.02$ and 0.03) ceramic powders was investigated after sintering. The sintering of the Sr-doped samples results in faster growth in particle-size and the shape becomes spherical by dissolution of the sharp edges in order to reduce the strain produced by Sr-doping and to reduce the surface energy. The growth in particle-size reduces the photocatalytic activity. Sr-doping reduces the band gap of ZnO by a small value (~ 0.1 eV). The ac conductivity values decrease with increase in Sr-concentration, but increase with temperature and frequency. This behavior is due to the conduction by small polarons created by Sr-doping. Our results may facilitate a way for the easy fabrication of monolithic ZnO based devices with improved dielectric and semiconducting properties of ZnO ceramics by doping a small amount of Sr.

1 Introduction

In semiconductor technology the modification in the properties of ZnO by the incorporation of dopant has become an important topic. Doping is a suitable method which yields remarkable changes in optical, electrical, morphological,

catalytic [1–9], magnetic and electronic properties of ZnO for important scientific and industrial applications [10, 11] such as piezoelectric transducers, optical wave guides, acoustic optic media, sensors, transparent conductive electrodes, varistors and solar cells etc [12, 13]. The incorporation of dopants improves the material properties depending on the type of dopants. The effect of dopant elements depend on its ionic radius and electronegativity [14]. It has been shown that doping of cations with bigger ionic radii than Zn^{2+} results in the creation of significant lattice defects due to the ionic radius mismatch between doped cation and Zn^{2+} ion [15]. In literature many reports are available for transition metal-, non-metal- and rare earth-doped ZnO for different applications [16] but still a very limited amount of research work on alkaline earth metal doped ZnO is available. However, alkaline earth metals are widely available in nature and have many military, industrial and biological applications [17]. Doping of Ca in ZnO is important for biological, optical, sensing and photonics applications [18]. Similarly, Mg and Ba are important for optical, antibacterial, sensing, photocatalysis and dielectric applications [19–23]. We note here that Sr is one of the important alkaline-earth metals which is widely used in many applications including electronics, metallurgy, chemical industry, military industry, optics etc. and is a potential candidate for doping in ZnO [17]. Recently, it has been reported that Sr doped ZnO is a promising candidate for the fabrication of sensor devices for monitoring indoor air quality [24], use in thin film transistors [25], improved photocatalytic activities [26], varistors [27], detection of ethanol vapour [28] and filtration applications [29]. Besides that, doping of ZnO with II-A elements, such as Ba, Sr and In etc., increase the n-type conductivity.

In the present work, $\text{Zn}_{1-x}\text{Sr}_x\text{O}$ ceramics were synthesized using a simple solid state reaction method with varying

✉ S. K. S. Parashar
sksparashar@yahoo.com; kparasharfch@kiit.ac.in

¹ School of Applied Sciences, Nano Sensor Lab, KIIT University, Bhubaneswar, Odisha 751024, India

² Materials Research Centre, Indian Institute of Science, Bangalore 560012, India

³ School of Physical Sciences, National Institute of Science Education and Research, Jatni 752050, India

Sr-dopant concentration. The effect of Sr doping on structural, photocatalytic and ac conductivity properties were investigated for $\text{Zn}_{1-x}\text{Sr}_x\text{O}$ samples with $x=0, 0.01, 0.02, 0.03$. The samples are labeled as P0, S1, S2 and S3, respectively. Additionally, in this paper we report the role of Sr as a sintering agent, however, the detailed mechanism has to be explored further. The ZnO ceramics doped with Ga were studied earlier for thermoelectric applications [30]. Although, bulk ceramic materials are important for the thermoelectric device fabrication, weak sinterability of Ga doped ZnO [31] is the major hindrance in this direction.

2 Experimental details

The Sr-substituted ZnO ($\text{Zn}_{1-x}\text{Sr}_x\text{O}$, $x=0, 0.01, 0.02$ and 0.03) ceramic samples were synthesized by solid state reaction method using high purity ZnO and SrCO_3 as precursors. The appropriate amounts of raw materials were ground in an agate mortar and pestle. The mixture was then calcined at 1100°C for 2 h (heating rate of $2^\circ\text{C}/\text{min}$). The obtained powder was characterized. We have also prepared pellets by pressing the powders (mixed with PVA binder) at a pressure of 437 MPa. The pressed pellets were then sintered at 1100°C for 2 h. The surface morphology and size of the particles in these pellets were studied. The surfaces of the pellets were then polished and electrodes were prepared with high purity silver paint and dried at 700°C for ~15 min for ac conductivity measurements.

The crystal structure, phase identification and determination of unit cell parameters of the calcined powder samples were performed via Rietveld refinement of the X-ray diffraction ($\text{Cu-K}\alpha$ radiation, $\lambda=1.5406 \text{ \AA}$) data measured at room temperature. The Rietveld refinement of the XRD patterns was performed by “FullProf” software [32]. The surface morphology was observed by Field Emission Scanning Electron Microscope (FESEM, Carl Zeiss NTS Ltd, UK). The catalytic activity of the calcined powders to degrade methylene blue was studied. The UV–Vis spectra were taken by “Lambda 750 UV/Vis/NIR Perkin Elmer” spectrophotometer in diffuse reflectance spectroscopy (DRS) mode for the powders and in transmission mode for the liquid methylene blue samples. The electrical properties of the pellets were studied using a computer controlled impedance analyzer (Hioki LCR Hi-tester-3532-50) over a wide range of frequencies (100 Hz to 1 MHz) and in a temperature range from RT to 500°C .

3 Results and discussion

3.1 Structural studies

The XRD patterns of the calcined $\text{Zn}_{1-x}\text{Sr}_x\text{O}$ ceramic powders are shown in Fig. 1 and the corresponding Rietveld

refinement results are given in Table 1. The analysis of the diffraction peaks revealed the hexagonal wurtzite structure of the samples for all the compositions (space group: $P6_3mc$). Absence of additional peaks in the XRD patterns indicates that the synthesized ceramics have single phase. This confirms the complete substitution of Sr^{2+} ions into the host material without affecting the crystal structure of ZnO [33]. However, the fitting of the XRD patterns according to a single phase (hexagonal $P6_3mc$) model was not satisfactory. A considerable shift of the peaks towards larger 2θ angle is seen along with asymmetry, as given in Fig. 1. Hence, the XRD patterns for the Sr-doped ($x=0.01, 0.02$ and 0.03) samples were fit using two phases having the same wurtzite structure but two different lattice parameters. One lattice parameter is due to the pure ZnO phase and the other (smaller) lattice parameter was assigned to the Sr-doped ZnO phase. This result suggests that little higher amounts ($>3 \text{ at\%}$) of Sr may be doped in ZnO. It can be observed from Table 1 that the amount of Sr-doped ZnO phase and the X-ray density of the samples increase with Sr-doping due to higher mass of Sr. We have used the Williamson–Hall (W-H) method to obtain the crystallite size and lattice strain present in all the samples, from the (FWHM) broadening of the XRD peaks [34]. The oxygen positional parameter (u) was calculated using the relation [35]:

$$u = \frac{1}{3} \left(\frac{a^2}{c^2} \right) + \frac{1}{4}$$

The u parameter is the relative displacement between Zn^{2+} and O^{2-} sublattice along the c -axis. The u parameter was found to increase when $\frac{c}{a}$ ratio decreased (Table 1). In wurtzite structure, the $\frac{c}{a}$ ratio deviates from the ideal value when bonding character becomes more ionic [35]. Considering the electronegativity of Sr (0.95) and Zn (1.65), doping with Sr increases the ionic character due to smaller electronegativity of Sr than Zn [36]. The bond length (Zn-O) reduces with Sr substitution which causes structural distortion in the crystal structure [36].

The dislocation density (δ) [37] and specific surface area (SSA) [38], were calculated using the following relation:

$$\delta = \frac{15\beta \cos \theta}{4aD}$$

$$\text{SSA} = \frac{6 \times 10^3}{D_p \cdot \rho}$$

where δ =dislocation density (/cc), β =broadening of diffraction line measured at half of its maximum (radian), θ =Bragg’s diffraction angle (radian), a =lattice constant (nm), D =crystallite size (nm), SSA = specific surface area, D_p =particle size (nm), ρ =density (g/cc) (Table 1).

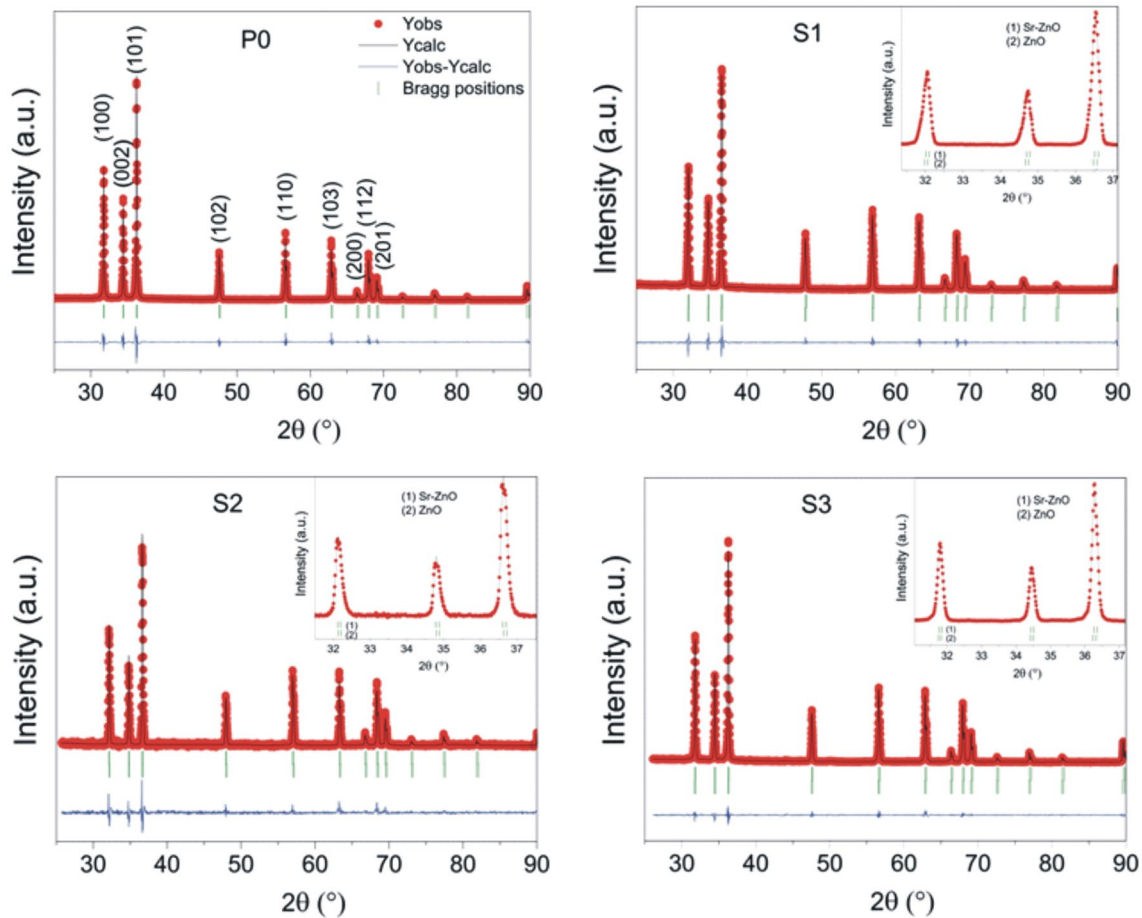


Fig. 1 XRD pattern of $Zn_{1-x}Sr_xO$ [P0 ($x=0$), S1 ($x=0.01$), S2 ($x=0.02$) and S3 ($x=0.03$)] ceramics

Table 1 The structural parameters obtained from the analysis of the Rietveld refinement results of the XRD patterns

Sample (wt% of Sr:ZnO)	a (Å)	c (Å)	a/c	ρ (g/cc)	$D_{Scherrer}$ (nm)	D_{SEM} (μm)	u	δ ($\times 10^{12}$) m^{-2}	SSA ($m^2 g^{-1}$)
P0 (0)	3.2495	5.2061	0.6242	5.657	101	1.15	0.37986	1.56778	0.9223
S1 (33.7)	3.2450	5.1962	0.6245	5.806	80	1.60	0.38000	2.50231	0.6459
S2 (50.0)	3.2463	5.1991	0.6244	5.874	77	1.75	0.38001	2.68341	0.5837
S3 (72.9)	3.2499	5.2059	0.6243	5.932	75	2.20	0.37991	2.83019	0.4598

D_{SEM} is the particle size obtained from the analysis of SEM micrographs. The numbers in the first column bracket are the weight fraction of the Zn-doped phase. The S1, S2 and S3 samples contain two ZnO phases: one is as listed and the other phase is the same as the pure phase ZnO (i.e., the parameters are same as that of P0 sample, 2nd row)

We have used the first three major peaks for the plane (100), (002), (101) for obtaining the values of the dislocation density and specific surface area for all ceramic samples as given in Table 1. The dislocation density increases with Sr-doping while the specific surface area decreases (Table 1). The decrease in specific surface area value indicates lower surface reactivity of the sample.

3.2 FESEM analysis

Figure 2 (left panel) displays the FESEM images of the $Zn_{1-x}Sr_xO$ powders calcined at 1100 °C. Significant changes in the morphology were observed with the variation of Sr concentration. For the undoped ZnO samples the particles are well dispersed and sizes are in 50–500 nm

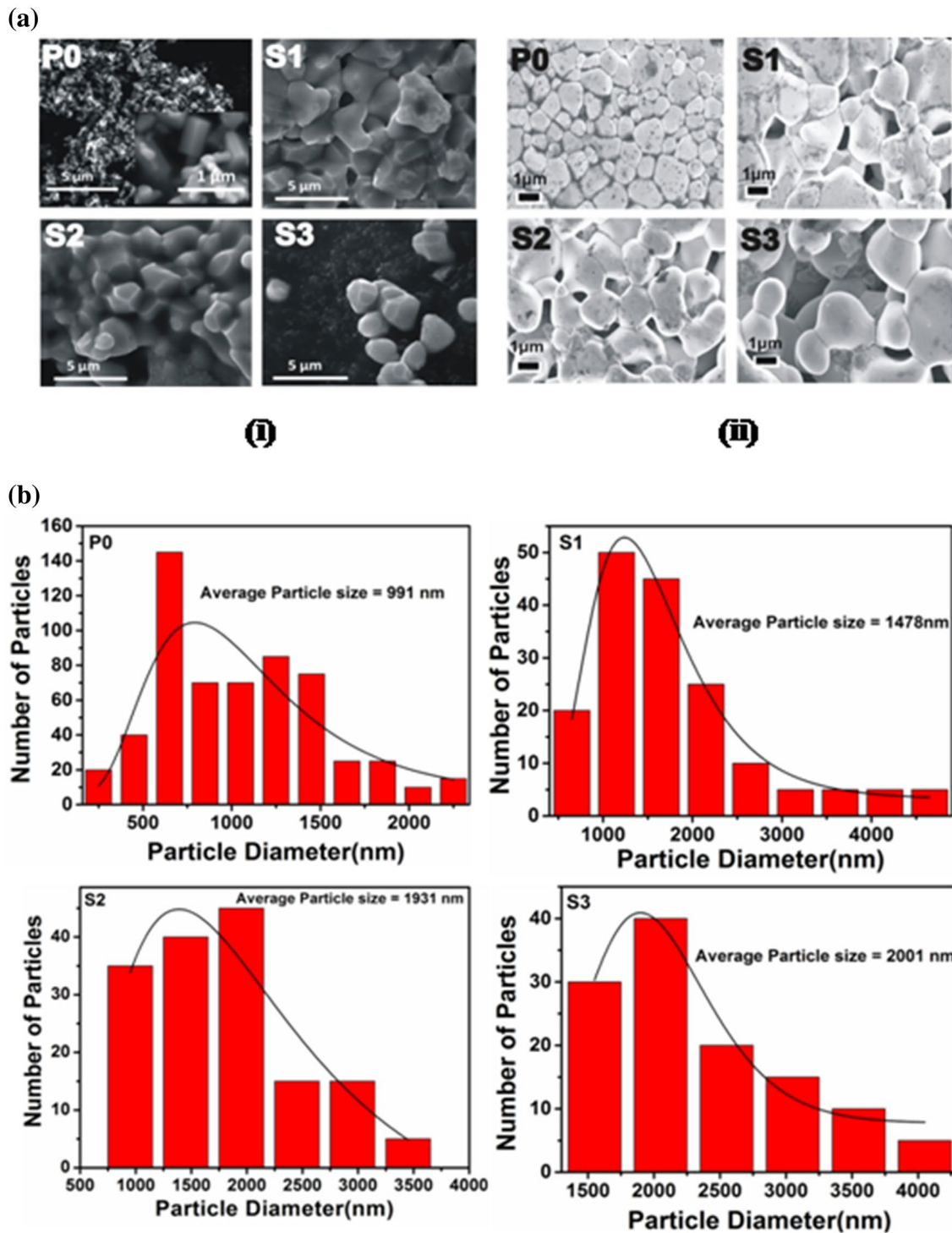


Fig. 2 **a** FESEM pattern of (i) calcined powders (ii) sintered pellets: $Zn_{1-x}Sr_xO$ [P0 ($x=0$), S1 ($x=0.01$), S2 ($x=0.02$) and S3 ($x=0.03$)] ceramics. **b** Particle size distribution of $Zn_{1-x}Sr_xO$ [P0 ($x=0$), S1 ($x=0.01$), S2 ($x=0.02$)] and S3 ($x=0.03$)

range with long hexagonal rod shaped grains. The morphology of the $x=0.01$ sample (S1) shows the growth of particle size to about 2–3 μm with the dissolution of sharp edges and a few of the particles agglomerate to form bigger

particles. But the connectivity among these agglomerates is not strong. The sample S2 shows particular morphology with better connectivity among the agglomerates (Ostwald ripening). Many such agglomerates are connected to form a

larger block. It is very interesting to see that with an addition of only about 2% of strontium, the morphology of the sample changes drastically, which suggests that the sinterability of the powder has increased by many folds. On further increase in Sr content to 3% (sample S3) the particles become big, spherical in shape and are well formed. Furthermore, the XRD results show that the grain growth has not occurred (Table 1). In fact the crystallite sizes were smaller than the undoped sample ZnO. This may be due to the strain produced by Sr doping (Table 1). Interestingly, it is surprising to see the fast growth of the agglomerates to form bigger particles just by an addition of few percent of Sr to ZnO.

In order to understand the role of Sr as a sintering agent, we pressed the calcined powders into pellets (described in experimental details). The pellets were sintered at 1100 °C for 2 h. It is clear from the FESEM images in Fig. 2 (right panel) that the particle sizes of the Sr doped samples increased tremendously, whereas the increase in particle size of the undoped ZnO sample is mediocre. This clearly demonstrates the enhancement of the sintering ability of ZnO, when a small amount of Sr is doped in ZnO. The origin of the lower sintering temperature with Sr doping has to be explored further.

3.3 UV–Vis diffuse reflectance spectroscopy (DRS) studies

Figure 3 shows the DRS of $\text{Zn}_{1-x}\text{Sr}_x\text{O}$ ceramic samples measured in the wavelength range of 250–800 nm. A sharp increase in band edge is observed at approximately 3.35 eV (370 nm) for all the samples. The optical band gap E_g of ZnO and doped ZnO was estimated by the Kubelka–Munk method [39]. The absorption coefficient (α) is related to the

reflectance via $F(R)$. Hence α is replaced by $F(R)$ in the calculations of Tauc plots.

$$F(R) = (1 - R)^2 / 2R$$

From Fig. 3 it was found that the band gap of ZnO decreased with about 1% of Sr doping, however, further increase in Sr content increases the band gap slightly. Overall there is very small change in the band gap in the investigated range of Sr doping. The variation in grain size, structural parameters, lattice strain, carrier concentration, presence of impurities (defects) and even deviation from stoichiometry are the factors responsible for the observed change in E_g .

3.4 Photocatalytic studies

To study the photocatalytic behavior of the synthesized samples (P0, S1, S2 and S3) we took 10 μM of methylene blue (MB) (4 ml) in separate vials. 100 mg of each sample was added to the respective vials and stirred for different intervals of time as indicated in Fig. 4 under (365 nm) UV irradiation. We observed rapid degradation of MB in case of ZnO while in case of doped samples the degradation proceeded slowly. Among the doped samples S1 showed higher photocatalytic behavior followed by S2 and S3. We can correlate this to the decreasing trend in SSA of $\text{S3} < \text{S2} < \text{S1} < \text{ZnO}$ (Table 1), as observed in FESEM images (Fig. 2). It is well known that a smaller particle size has larger surface area and thus the catalytic activity is higher for them. It was shown [15] that Sr-doped ZnO prepared by sol–gel route shows reduction in the particle size as the Sr-content increases. This in turn enhanced the photocatalytic activity of those particles approximately by two times. But in our case, where the samples were prepared by solid state reaction route, the particle size increased by many fold and the surface area for catalytic reaction decreased leading to a drastic decrease in catalytic behavior, as will be discussed below.

We studied the rate of degradation of MB under UV irradiation using the UV–Vis spectrophotometer. In a typical experiment 100 ml of 2 μM MB dye was taken in two separate beakers. 100 mg of the ZnO (P0) sample was added to one beaker, while 100 mg of the sample S1 was added to the other. The mixtures were stirred in dark conditions for 30 min, for complete adsorption. Each of these mixtures was illuminated with (365 nm) UV radiation for 1 h. 5 ml of the dye was repeatedly pipetted out and filtered in test tubes at different time intervals. The absorbance of the filtrate was measured in the UV–Vis spectrophotometer. The plot of absorbance versus wavelength for ZnO (P0) is shown in Fig. 4a. Figure 4b shows the exponential decay in the concentration of MB for P0 and S1 particles as catalysts. The calculated rate of degradation for pure ZnO

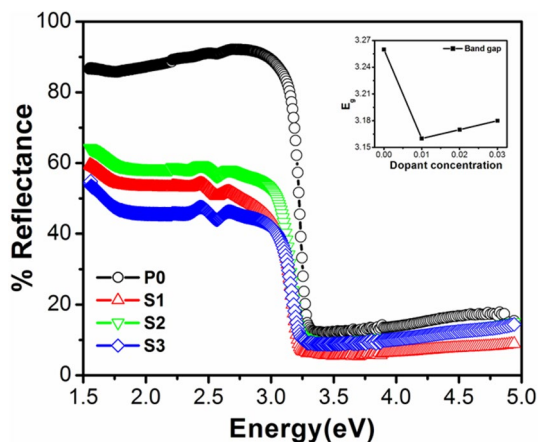


Fig. 3 UV–Vis diffuse reflectance spectra of calcined powders of $\text{Zn}_{1-x}\text{Sr}_x\text{O}$ [P0 ($x=0$), S1 ($x=0.01$), S2 ($x=0.02$) and S3 ($x=0.03$)] (inset band gap variation with dopant concentration)

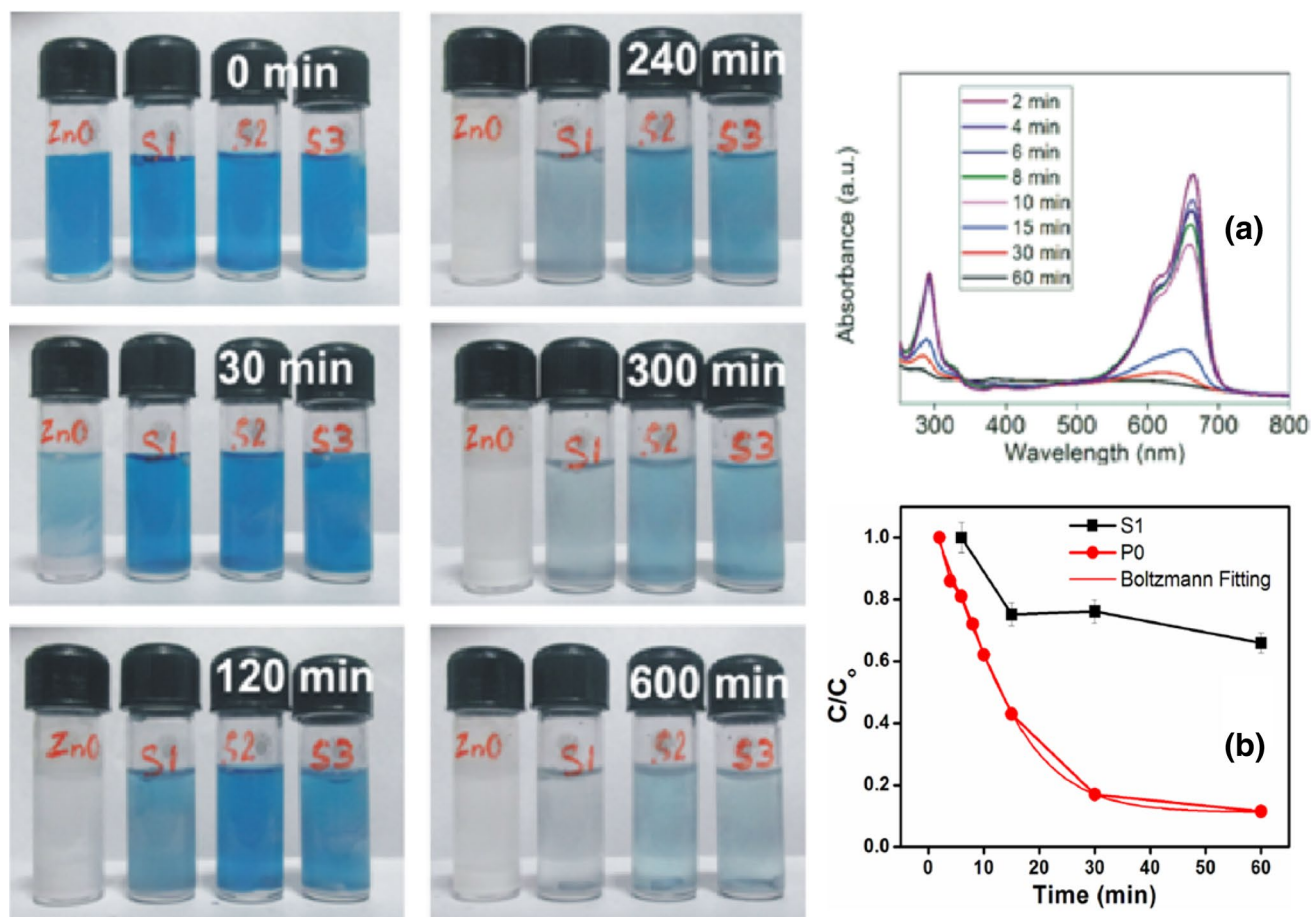


Fig. 4 Demonstration of photocatalytic degradation of methylene blue (a), photocatalytic degradation of methylene blue by ZnO (b). Exponential decay curves of MB degradation by ZnO and S1

powder, P0 (as catalyst) was 0.056 min^{-1} , while that for S1 was 0.007 min^{-1} . The decay curve clearly shows more efficient catalytic behavior of ZnO than the Sr-doped sample (S1). The detailed mechanism of photocatalytic activity of ZnO is studied earlier [40].

3.5 AC conductivity studies

Conductivity measurements were carried out to understand the conduction mechanism in the investigated frequency regime. Generally the total conductivity can be expressed as [41]:

$$\sigma_{tot.} = \sigma_0(T) + \sigma(\omega, T)$$

Here, first term on right hand side is the dc conductivity due to band conduction which is independent of frequency. The second term is pure ac conductivity due to the hopping of charge carriers between the metal ions. We have used the sintered pellets for ac conductivity measurements. The variations of ac conductivity with frequency at selected temperatures are shown in Fig. 5.

The ac conductivity pattern shows a progressive rise in conductivity with increase in temperature, indicating the negative temperature co-efficient of resistance (NTCR) of the samples. Figure 5 shows that the conductivity values of the Sr-doped samples are less than that of the undoped ZnO sample. It may be due to the densification achieved by Sr substitution into ZnO lattice.

Furthermore, with increase in dopant concentration, the conductivity decreases. In general, the frequency response of $\sigma_{ac}(\omega)$ can be explained by hopping or polaron mechanism [42] based on the availability of free charge carriers in the system. On application of electric field, the motion of electrons in oxide materials tends to distort/polarize the surrounding lattice to form polarons. Large polarons normally account for the variation of decreased σ_{ac} with increase in frequency, whereas for small polarons the σ_{ac} increases with increase in frequency. It is clear from the figure that the observed increase in σ_{ac} with the increase in frequency confirms the conduction mechanism arising due to small polaron mechanism.

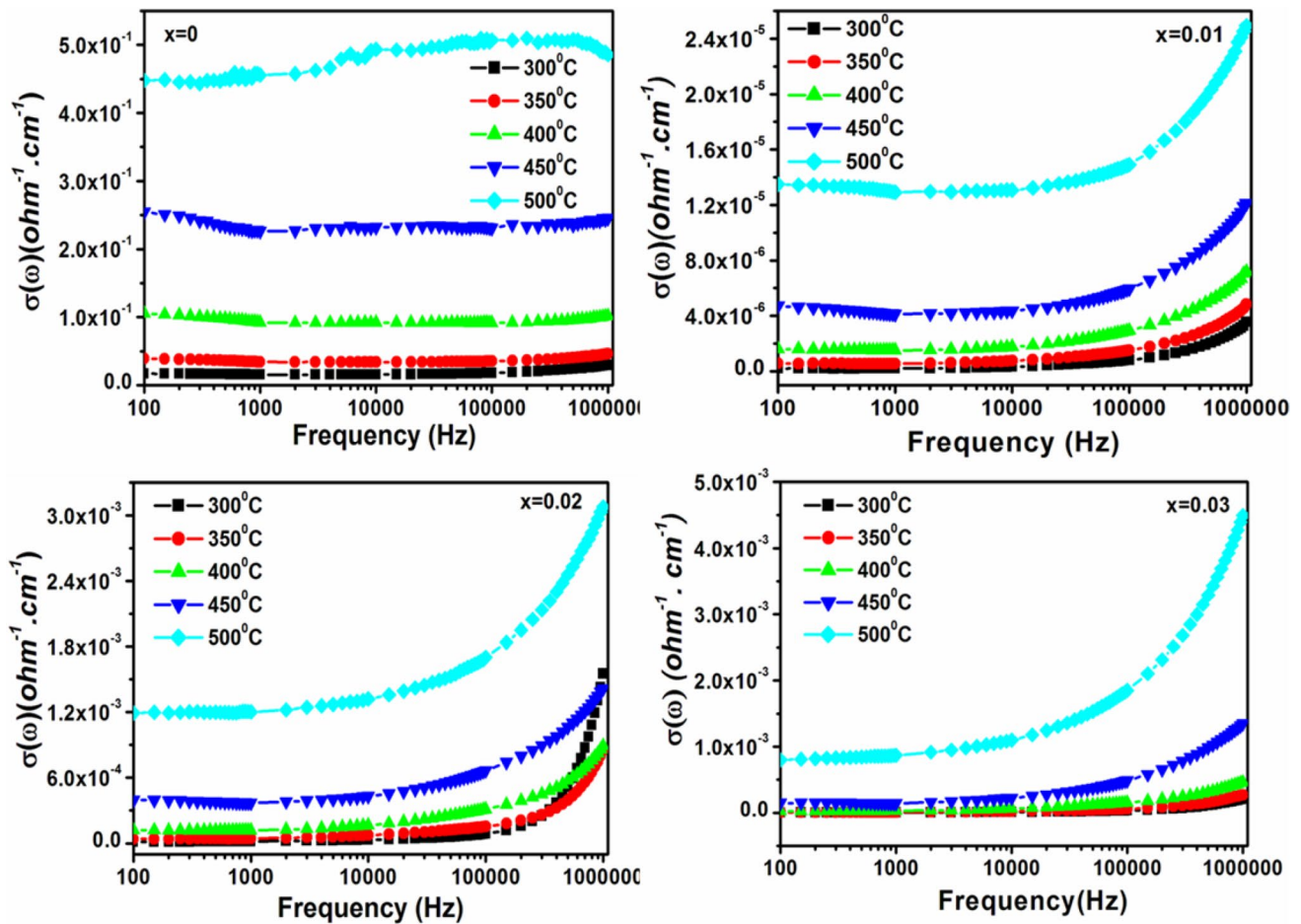


Fig. 5 Variation of ac conductivity of $Zn_{1-x}Sr_xO$ ($x=0, 0.01, 0.02$ and 0.03) ceramics with frequency

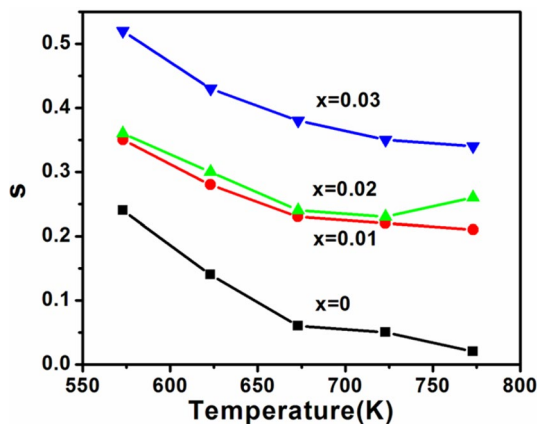


Fig. 6 Variation of exponent s of $Zn_{1-x}Sr_xO$ ($x=0, 0.01, 0.02$ and 0.03) ceramic samples with temperature

With the increase in temperature, the conductivity was found to increase in all cases shown in Fig. 6 which can be attributed to the free as well as bound carriers from different regions in ceramics such as grain and grain boundaries

that are distributed inhomogeneously. This leads to a change in activation energy with temperature. These charge carriers may arise from Sr ion dopants or oxygen vacancies. The frequency dependent ac conductivity results (explained below) confirm that the present system has semiconducting nature along with NTCR behavior.

The frequency-dependent conductivity increases approximately linearly with frequency as $\sigma(\omega) = A\omega^s$ ($0 < s < 1$) [43]. The exponent “s” is estimated from the slope of $\ln\sigma_{ac}(\omega)$ versus $\ln(\omega)$ is shown in Fig. 7. The observed dependence of the variation of exponent(s) values on temperature is a strong evidence for thermally activated polarization mechanism [44]. The values of s are found to decrease for all the compositions with increase in temperature. We have determined activation energy by the use of Arrhenius equation [45], $\sigma_{ac} = \sigma_0 \exp(-E_a/K_B T)$, where, E_a is the activation energy for the conduction of the ions, K_B is the Boltzmann constant, T is the measurement temperature and σ_0 is the pre-exponential factor. The activation energy E_a for P0, S1, S2 and S3 samples ($x=0, 0.01, 0.02$ and 0.03 , respectively) were evaluated at different

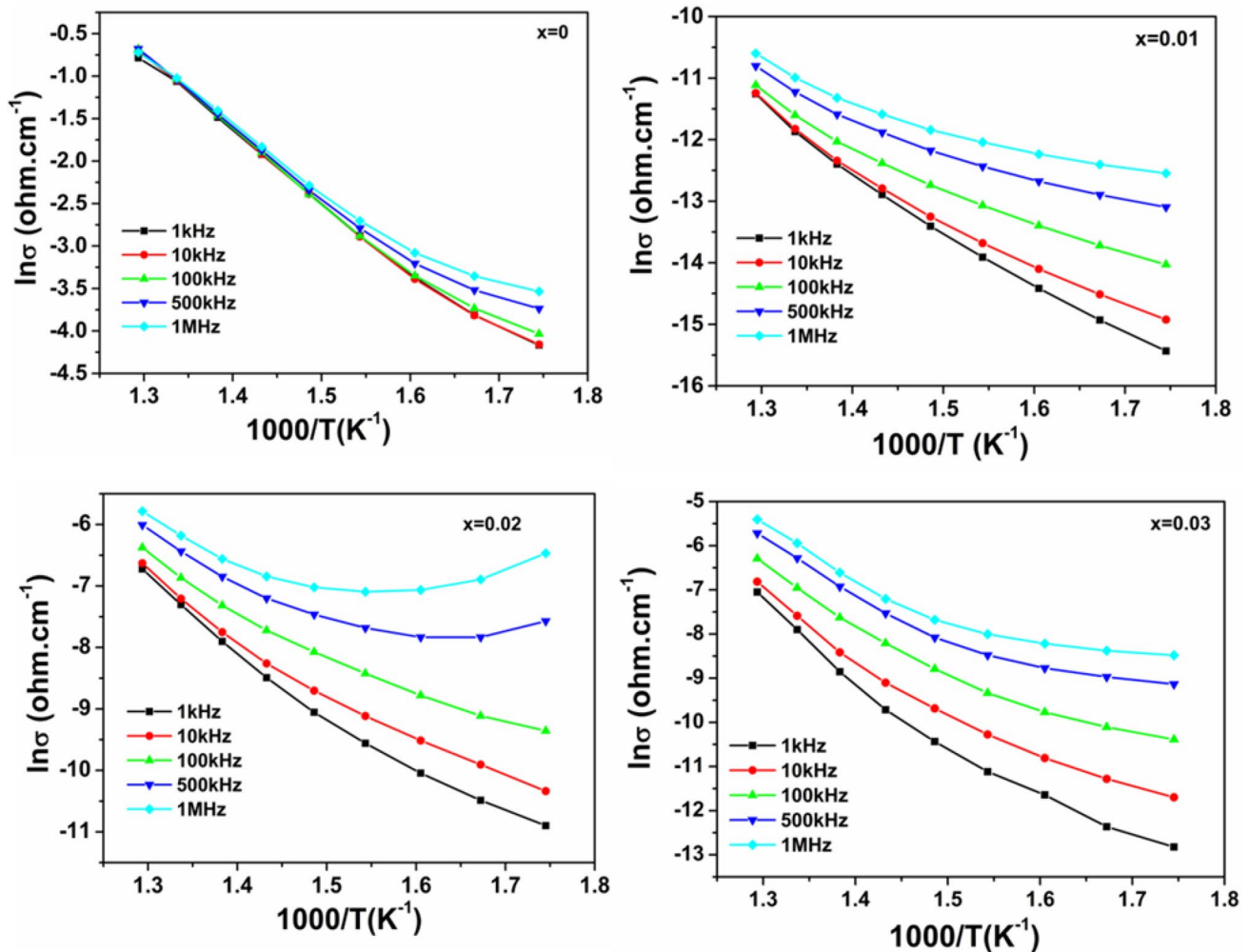


Fig. 7 Variation of ac conductivity of $Zn_{1-x}Sr_xO$ ($x=0, 0.01, 0.02$ and 0.03) samples with inverse of temperature

frequency is shown in Fig. 8. The increasing trend of activation energy is due to the increased effective collision per unit volume as the doping of Sr increases.

4 Conclusions

Phase pure Sr-doped ZnO polycrystalline powder ($Zn_{1-x}Sr_xO$) was synthesized by solid state reaction technique. The effect of Sr-substitution on the lattice parameters, dislocation density and u -parameter were obtained using Rietveld refinement of the XRD patterns. The Rietveld refinement of XRD patterns suggests that Sr atoms substitute Zn sites in the crystal without any modification to the wurtzite structure but the lattice parameter changes slightly with Sr-substitution. Sr acts as a sintering agent, which makes the particles grow bigger and become more spherical in shape. A small decrease in band gap after Sr-doping was observed. The catalytic activity of the Sr-doped

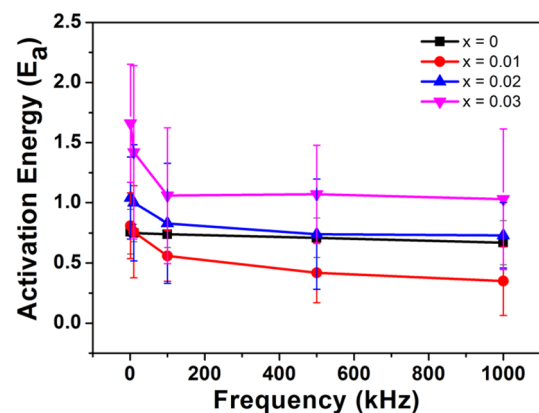


Fig. 8 Variation of activation energy of $Zn_{1-x}Sr_xO$ ($x=0, 0.01, 0.02$ and 0.03) samples with frequency

samples decreases due to growth of particles in size. The ac conductivity values decrease with Sr-doping making the Sr-doped ZnO sample a better dielectric material than pure ZnO. The temperature dependent ac-conductivity results confirmed the small polaron-based conduction mechanism. Furthermore, the conductivity increases with increases in temperature and also with increase in frequency, which is better for dielectric applications. Our results on enhanced sinterability of ZnO by a small addition of Sr may help in fabricating various optoelectronic and thermoelectric devices without compromising the semiconducting (band gap) and dielectric properties of ZnO.

References

- D.A. Reddy, R. Ma, M. Yong Choi, T.K. Kim, *Appl. Surf. Sci.* **324**, 725–735 (2015)
- D.A. Reddy, J. Choi, S. Lee, R. Ma, T.K. Kim, *RSC Adv.* **5**, 18342–18351 (2015)
- D.A. Reddy, S. Lee, J. Choi, S. Park, R. Ma, H. Yang, T.K. Kim, *Appl. Surf. Sci.* **341**, 175–184 (2015)
- D.A. Reddy, J. Choi, S. Lee, R. Ma, T.K. Kim, *RSC Adv.* **5**, 67394–67404 (2015)
- J. Choi, D.A. Reddy, T.K. Kim, *Ceram. Int.* **41**, 13793–13803 (2015)
- M.J. Islam, D.A. Reddy, N.S. Han, J. Choi, J.K. Song, T.K. Kim, *Phys. Chem. Chem. Phys.* **18**, 24984–24993 (2016)
- J. Choi, D.A. Reddy, M.J. Islam, R. Ma, T.K. Kim, *J. Alloys Compd.* **688**, 527–536 (2016)
- D.A. Reddy, J. Choi, S. Lee, T.K. Kim, *J. Taiwan. Inst. Chem. Eng.* **66**, 200–209 (2016)
- S. Lee, D.A. Reddy, T.K. Kim, *RSC Adv.* **6**, 37180–37188 (2016)
- R.A. Zargar, M. Arora, M. Ahmad, A.K. Hafiz, *J. Mater.* **2015**(1), 1–6 (2015)
- A. Zia, S. Ahmed, N.A. Shah, M. Anis-ur-Rehman, E.U. Khan, M. Basit, *Phys. B* **473**, 42–47 (2015)
- R. Yogamalar, A. Bose, *Synth. Prog. Nanotechnol. Nanomater.* **2**, 1–20 (2013).
- S. Xu, Z.L. Wang, *Nano Res.* **4**, 1013 (2011)
- D.K. Vinod Kumar, S. Suman, S. Kumar, *AIP Conf. Proc.* **1728**, 020458, (2016)
- R. Yousefi, F. Jamali-Sheini, M. Cheraghizade, S. Khosravi-Gandomani, A. SÁaedi, N.M. Huang, W.J. Basirun, M. Azarang, *Mater. Sci. Semicond. Process.* **32**, 152–159 (2015)
- T. Das, B.K. Das, K. Parashar, S.K.S. Parashar, *Bull. Mater. Sci.* **40**, 247–251 (2017)
- D. Li, J.F. Huang, L.Y. Cao, J.Y. Li, H.B. Ouyang, C.Y. Yao, *Ceram. Int.* **40**, 2647–2653 (2014)
- T. Das, B.K. Das, K. Parashar, S.K.S. Parashar, *Acta Phys. Pol. A* **130**, 1358–1362 (2016)
- J. Iqbal, T. Jan, M. Ismail, N. Ahmad, A. Arif, M. Khan, M. Adil, S. Sami-Ul-Haq, A. Arshad, *Ceram. Int.* **40**, 1493–1487 (2014)
- Y. Liu, T. Hang, Y. Xie, Z. Bao, J. Song, H. Zhang, E. Xie, *Sens. Actuators B* **160**, 266–270 (2011)
- R. Zamiri, B. Singh, I. Bdkin, A. Rebelo, M. Scott Belsley, J.M.F. Ferreira, *Solid State Commun.* **195**, 19–74 (2014)
- V.K. Etacheri, R. Roshan, V. Kumar, *ACS Appl. Mater. Interfaces* **4**, 2715–2717 (2012)
- L.H.S. Lacerda, S.R. de Lazaro, R.A.P. Ribeiro, *IOP Conf. Series* **97**(1–6), 012005 (2015)
- P.M. Shirage, A.K. Rana, Y. Kumar, S. Sen, S.G. Leonardi, G. Neri, *RSC Adv.* **6**, 82733–82742 (2016)
- W. Shao-Hang, Z. Nan, H. Yong-sheng, C. Hang, J. Da-Peng, *Chin. Phys. B* **24**, 108504 (2015)
- K. Pradeev Raj, K. Sadaiyandi, A. Kennedy, R. Thamizselvi, *Mater. Chem. Phys.* **183**, 24–36 (2016)
- K. Gunturkun, H.O. Toplan, *Ceram. Silikaty* **50**, 225–231 (2006)
- T.A. Vijayan, R. Chandramohan, S. Valanarasu, J. Thirumalai, S.P. Subramanian, *J. Mater. Sci.* **43**, 1776–1782 (2008)
- W. Water, Y.S. Yan, *Thin Solid Films* **515**, 6992–6996 (2007)
- G.K. Paul, S.K. Sen, *Mater. Lett.* **57**, 742–746 (2002)
- B.A. Cook, J.L. Harringa, C.B. Vining, *J. Appl. Phys.* **83**, 5858 (1998)
- J. Rodriguez-Carvajal, *Phys. B* **192**, 55–69 (1993)
- S. Singhal, J. Kaur, T. Namgyal, R. Sharma, *Phys. B* **407**, 1223–1226 (2012)
- M. Arshad, A.S. Ahmed, A. Azam, A.H. Naqvi, *J. Alloys Compd.* **577**, 469–474 (2013)
- U. Özgür, Y.I. Alivov, C. Liu, A. Teke, M.A. Reshchikov, et al., *J. Appl. Phys.* **98**(1–103), 041301 (2005)
- P. Kumar, Y. Kumar, H.K. Malik, S. Annapoorni, S. Gautam, K.H. Chae et al., *Appl. Phys. A* **114**, 453–457 (2014)
- R. John, R. Rajakumari, *Nano-Micro Lett.* **4**, 65–72 (2012)
- A. Sahai, N. Goswami, *Phys. E* **58**, 130–137 (2014)
- T. Badapanda, S. Sarangi, B. Behera, S. Parida, S. Saha, T.P. Sinha, R. Ranjan, P.K. Sahoo, *J. Alloys Compd.* **645**, 586–596 (2015)
- S. Adhikari, R. Gupta, A. Surin, T. Satish Kumar, S. Chakraborty, D. Sarkar, G. Madras, *RSC Adv.* **6**, 80086–80098 (2016)
- A. Ghosh, N. Kumari, S. Tewari, A. Bhattacharjee, *Mater. Sci. Eng. B* **196**, 7–14 (2015)
- B. Dhanalakshmi, P. Kollu, B.P. Rao, P.S.V.S. Rao, *Ceram. Int.* **42**, 2186–2197 (2016)
- S.S.N. Bharadwaja, P. Victor, P. Venkateswarulu, S.B. Krupani-dhi, *Phys. Rev. B.* **65**(1–9), 174106 (2002)
- S. Bhandari, N. Sinha, B. Kumar, *Ceram. Int.* **42**, 4274–4284 (2016)
- Y.P.V. Subbaiah, P. Prathap, K.T.R. Reddy, *Appl. Surf. Sci.* **253**, 2409–2415 (2006)